The Dynamical Properties of Three Different Variants of the Orange Carotenoid Protein: A Quasielastic Neutron Scattering Study

Mina Hajizadeh [1], Maksym Golub [1], Marcus Moldenhauer [2], Wiebke Lohstroh [3], Thomas Friedrich [2] and Jörg Pieper [1,*]

1 Institute of Physics, University of Tartu, 50411 Tartu, Estonia; mina.hajizadeh@ut.ee (M.H.); maksym.golub@ut.ee (M.G.)
2 Institute of Chemistry PC 14, Technische Universität Berlin, Straße des 17. Juni 135, 10623 Berlin, Germany; marcus.moldenhauer@tu-berlin.de (M.M.); friedrich@chem.tu-berlin.de (T.F.)
3 Heinz Maier-Leibnitz Zentrum (MLZ), Technische Universität München, Lichtenbergstraße 1, 85748 Garching, Germany; wiebke.lohstroh@frm2.tum.de
* Correspondence: pieper@ut.ee; Tel.: +372-737-4627

Abstract: Besides a well-adapted structure, proteins often require a specific dynamical flexibility to undergo conformational changes in order to carry out their function. The latter dynamics can be directly measured by quasielastic neutron scattering as demonstrated here for three variants of the orange carotenoid protein (OCP), which plays a pivotal role in the protection of the cyanobacterial photosynthetic apparatus against photodamage. We investigate the dynamics of the structurally compact, dark-adapted wild type of OCP (OCP^{wt}) in comparison with that of two mutant forms. The latter two mutants differ preferentially in their structures. The orange mutant OCP-W288A is assumed to have a compact structure and to preferentially bind the pigment echinenone, while the pink mutant OCP-W288A appears to represent the more elongated structure of the red active state of OCP binding the carotenoid canthaxanthin, respectively. The study reveals three major findings: (a) the dynamics of the red active state of OCP is significantly enhanced due to a larger number of protein residues being exposed to the solvent at the surface of the protein; (b) the dynamics of all OCP forms appear to be suppressed upon the freezing of the solvent, which is most likely due to an ice-induced aggregation of the proteins; and (c) the wild type and the compact mutant exhibit different dynamics attributed to a missing H-bond between the pigment and protein, resulting a destabilization of the surrounding protein.

Keywords: photoprotection; orange carotenoid protein; protein dynamics; quasielastic neutron scattering

1. Introduction

Light-harvesting is a highly efficient process performed by dedicated photosynthetic protein complexes [1]. In the case of light stress, however, reactive oxygen species (ROS) such as singlet oxygen ($^1O_2$) may be formed, which can damage the photosystem and lead to cell death [2]. Therefore, regulatory mechanisms are necessary to protect the photosynthetic apparatus from damage caused by excessive light absorption [3,4]. The mechanisms that respond to light-intensity variations incident on the plant's photosynthetic apparatus involve rapid and slow changes in its structure and function [5]. Cyanobacteria are known for using phycobilisomes (PBSs) as their primary light-harvesting antennae, and exhibit a photoprotective mechanism referred to as non-photochemical quenching (NPQ) [6,7]. NPQ in cyanobacteria requires the orange carotenoid protein (OCP) to act as a high-light sensor [8]. The OCP effectively dissipates excess solar energy after binding to PBSs, thus mitigating oxidative stress and photo-induced damage [9]. The OCP is the only photo-sensory protein described so far with carotenoids acting as active chromophores [10]. The

OCP is a 35 kDa water-soluble protein consisting of an α/β-fold C-terminal domain (CTD) and an α-helical N terminal domain (NTD) connected by a flexible linker (Figure 1) [11]. In the dark-adapted state, the two domains are connected through (1) an N-terminal extension (NTE, residues 1–15), binding to the primary β-sheet of the CTD; (2) a flexible linker between the two domains (residues 166–189); (3) a salt bridge between the residues Arg155 and Glu244; and (4) through the keto-carotenoid found in the cavity between two domains [12]. Recent studies have indicated that the OCP can bind 3′-hydroxyechinenone (3′-hECN), canthaxanthin (CAN), and echinenone (ECN) by forming H-bonds with the 100% conserved CTD amino acids Y201 and W288. The absorption of blue light by the OCP induces a photocycle, converting the dark-adapted orange form OCP^O into the active, red form OCP^R, following significant structural changes. OCP^R is able to bind to the PBS antenna and induce the conversion of excess energy into heat by NPQ [13].
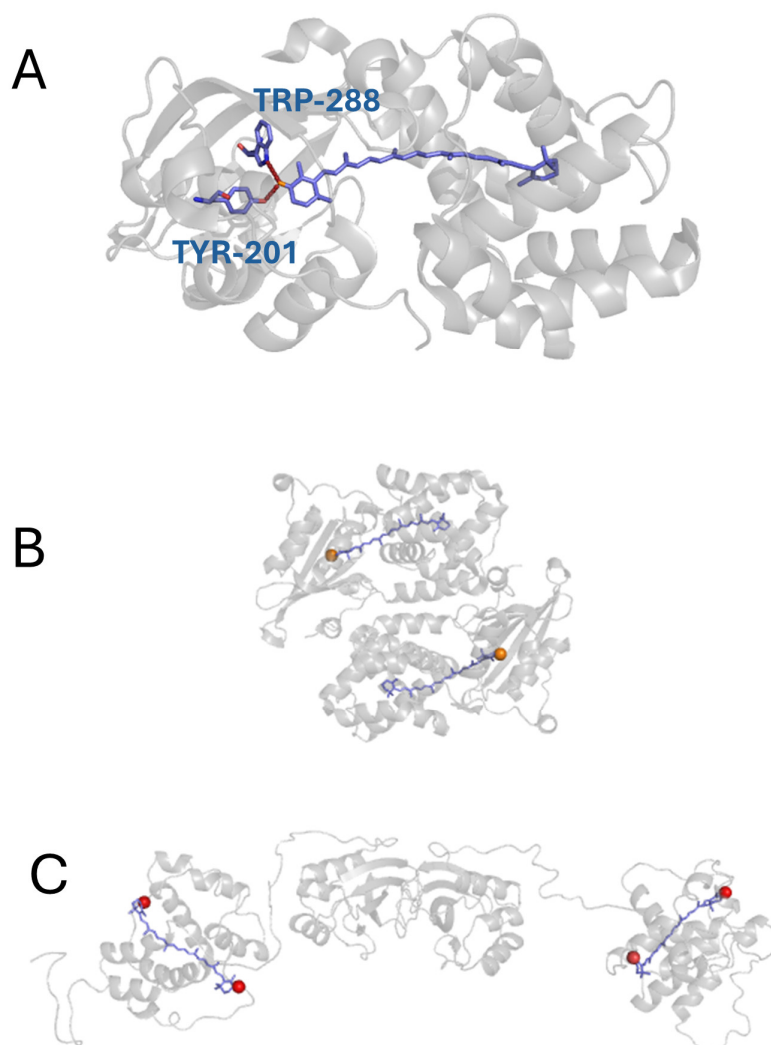

Figure 1. Panel (**A**): X-ray structure of OCP^O (PDB 7qd0) [11] with echinenone as the bound carotenoid and indicating the two H-bonds formed with the protein. Panel (**B**): Pepsi structure of the mutant OCP^{MO} based on the small angle scattering data of OCP^O based on Golub et al. [14] but modelled with echinenone as the bound carotenoid (**B**), respectively. Panel (**C**): Pepsi structure of the mutant OCP^{MP} based on the small angle scattering data of OCP^{W288A} based on Golub et al. [14] but modelled with canthaxanthin as the bound carotenoid. The carbonyl groups capable of forming hydrogen bonds with the solvent are shown as orange and red spheres, respectively. Molecular graphics in Figure 1 are created by Pymol (the Pymol Molecular Graphics System, version 2.0, Schrödinger, LLC, New York, NY, USA).

The exact mechanism that triggers the conversion of OCP^O to OCP^R requires further exploration, but appears to involve the breaking of H-bonds between the carotenoid and the protein, and a shift of the carotenoid to the NTD [15–17]. This is followed by the unfolding of the N-terminal extension (NTE) along with its separation from the CTD [18] and by the subsequent separation of the two protein domains [11,19]. However, the high-resolution structure of OCP^R had not been available until recently. In contrast, low-resolution structures of OCP^O and OCP^R were reported based on small angle X-ray and neutron scattering (SAXS and SANS) experiments [14,20,21]. In solution, both OCP forms, in its active or dark-adapted state, were preferentially found in dimeric form even at low concentrations [14]. More recently, cryo-electron microscopy revealed detailed insights into the structure of the active state OCP^R as part of the entire quenched OCP-PBS super-complex from *Synechocystis* sp. PCC 6803 at a resolution of 2.7 Å [22]. The latter study also reports a dimeric OCP^R structure with separated domains and with the carotenoid located within the NTD.

In addition to structural properties, the flexibility of proteins is widely acknowledged as a crucial factor for their functional capabilities [23]. This is particularly true for proteins like OCP, which rely on significant structural changes for their intended functions; see below. The relationship between dynamics and function is often inferred by observing the simultaneous suppression or cessation of conformational protein motions and biological activity at characteristic temperatures or hydration levels. For example, specific electron-transfer steps are hindered in photosynthetic reaction centers when the temperature is lowered, indicating the necessity of conformational protein dynamics for these processes [24–26].

Quasielastic neutron scattering (QENS) is a powerful analytical tool used in biology that provides valuable insights into the vibrational and conformational dynamics of biological molecules, such as proteins and lipids, in solution [23,27–29]. QENS is particularly useful due to the significant scattering cross-section of hydrogen atoms, which are uniformly distributed in biomolecules. Consequently, it is extensively employed for studying molecular motions in proteins. QENS experiments have revealed that proteins and biological membranes exhibit hydration-dependent conformational dynamics at physiological temperatures above a specific dynamical transition, typically occurring within the temperature range of 200 to 240 K [24,25,30–33], depending on the specific protein and its environment.

The active state OCP^R does not only possess a largely altered structure, but also exhibits a specific protein flexibility also known as a "molten globule" state [34,35]. A significantly enhanced protein flexibility of the active state OCP^R was then subsequently observed in QENS experiments mainly carried out at room temperature [36,37]. However, no detailed temperature dependence of the latter effect has been investigated, so many questions regarding the origin of the dynamics and concerning the role of the solvent are still lingering.

Here, we employ QENS experiments to study the dynamics of three different OCP samples over a wide temperature range between 100 and 300 K. As a reference, we use wild-type OCP, representing the structurally compact, dark-adapted form (hereafter referred to as OCP^{wt}). In addition, we use two different samples with point mutations at position W288 to generate two OCPs, which differ in their structure and in carotenoid content. OCP-W288A-orange has a compact structure similar to OCP^O and contains preferentially ECN, while OCP-288A-pink has an elongated structure similar to that of the active state OCP^R and binds mainly to CAN. For illustration, comprehensive structural models of the latter two forms are shown in Figure 1, which are based on the low-resolution small angle scattering data of Golub et al. [14]. The absorption spectra of the two mutants shown in Figure 2 are similar to those of the dark-adapted and active states OCP^O and OCP^R, respectively, supporting the structural models shown in Figure 1. OCP-W288A-orange and OCP-288A-pink will hereafter be referred to as OCP^{MO} (OCP mutant orange) and OCP^{MP}

(OCP mutant pink). This study reveals essential information for a deeper understanding of the role of protein dynamics in the regulation of photosynthetic processes.
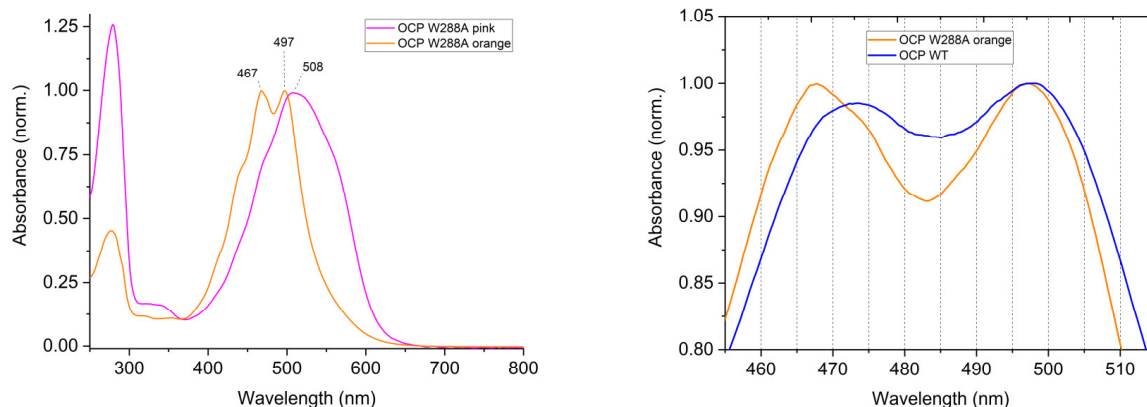

Figure 2. Comparison of absorption spectra of the mutants OCP W288A orange and pink, respectively. (**Left panel**): the spectrum of OCP W288A pink (OCP^{MP}) with a peak at about 508 nm is red-shifted, similar to that of the active state of OCP^{R}. In contrast, the spectrum of OCP W288A orange (OCP^{MO}) with peaks at 467 and 497 nm is rather similar to that of OCP wild type. (**Right panel**): direct comparison of the peak region of the spectra of OCP wild type and OCP W288A orange (OCP^{MO}).

2. Material and Methods

2.1. Sample Preparation

The sample preparation including DNA cloning, protein purification, and pigment analysis was described in detail before in [37]. Briefly, the cloning of DNA resulted in the plasmid pRSFDuetM-OCP or pRSFDuetM-OCP W288A, which also encodes all genes for producing β-carotenes, including ECN and CAN. For the separation of orange and pink protein variants, a hydrophobic-interaction chromatography (HIC) was used. After protein purification, the buffer was exchanged from H_2O to D_2O to suppress the solvent scattering in the QENS experiments, achieving a D_2O content of 99.9%. The final protein concentration was around 50 mg/mL. The pigment analysis revealed that the wild-type OCP^{wt} contains about 99% ECN, the mutant OCP^{MO} binds to about 85% of ECN, and OCP^{P} contains about 92% CAN. Absorption spectra were recorded using a Maya2000pro spectrometer (Ocean Insight, Orlando, FL, USA) coupled by a fiber to a deuterium tungsten light source (Sarspec, Vila Nova de Gaia, Portugal) and a cuvette holder (CVH100, Thorlabs, Bergkirchen, Germany).

2.2. QENS Experiments

The QENS spectra of 3 different OCPs (OCP^{wt}, OCP^{MO}, and OCP^{MP}) were measured over a wide range of temperatures between 100 and 300 K using the time-of-flight spectrometer Tof-Tof (Heinz Maier-Leibnitz Zentrum, MLZ, in Garching, Germany). The incident neutron wavelength was 5 Å with an elastic resolution ΔE of 75 µeV, which corresponds to a wide observation time range from 0.1 ps to 26 ps. The respective elastic Q range was 0.25 to 2.3 Å^{-1}. The chopper speed was set to 14,000 rotations per minute, with a frame-overlap chopper ratio of 4. The raw data were normalized and corrected for the empty cell contribution and detector efficiency before being transferred to the energy and momentum transfer scale using the program package Mantid [38].

We investigated three different OCP forms, each having a volume of 1 mL and a protein concentration of approximately 65 mg/mL. To precisely evaluate the influence of the solvent scattering, we performed separate experiments using the sole buffer solution; see below.

2.3. QENS Data Analysis

The data analysis procedure described in detail before in [37] involves an experimental scattering function of a protonated scatterer,

$$S_{exp}(Q,\omega) = F_N \exp\left(-\frac{\hbar\omega}{2kT}\right) R(Q,\omega) \otimes S_{theo}(Q,\omega) \qquad (1)$$

consisting of a normalization factor F_N, the detailed balance factor outlined by $\exp\left(-\frac{\hbar\omega}{2kT}\right)$, and the resolution function $R(Q,\omega)$, and the model scattering functions $S_{theo}(Q,\omega)$ are both functions of energy $\hbar\omega$ and the momentum transfer vector Q. The model function characterizing the protein's dynamics is often used as follows:

$$S_{theo}(Q,\omega) = e^{-\langle u^2 \rangle Q^2}\left\{ A_0(Q)\delta(\omega) + \sum_n A_n(Q)L_n(H_n,\omega) + S_{in}(Q,\omega) \right\} \qquad (2)$$

containing the Debye–Waller factor $e^{-\langle u^2 \rangle Q^2}$ with the "global" vibrational mean square displacement $\langle u^2 \rangle$ and the elastic component $A_0(Q)\delta(\omega)$, followed by the quasielastic component $\Sigma A_n(Q)L_n(H_n, \omega)_n$, and, finally, the (vibrational) inelastic contribution $S_{in}(Q, \omega)$. Assuming an exponential protein relaxation, the line shape $L_n(H_n, \omega)$ becomes a Lorentzian with a width (H_n, HWHM) related to a characteristic relaxation time τ_R. The relaxation time is inversely proportional to the width of the line shape, meaning that as the width of the line shape increases, the relaxation time decreases. The pre-factors $A_0(Q)$ and $A_n(Q)$ are elastic and quasi-elastic incoherent structure factors (*EISF* and *QISF*), respectively, which are normalized to unity according to the following:

$$\sum_n A_n(Q) = 1 - A_0(Q). \qquad (3)$$

According to Equation (2), each QENS spectrum was fitted using a sum of one elastic contribution and a number of Voigt functions. The experimental resolution was defined according to the fit of the vanadium spectrum and was fixed in all further fits. The latter two components are referred to as slow (narrow linewidth) and fast components (broad linewidth), respectively.

The jump-diffusion model of protons is used to describe the protein's slow component. Following the Singwi and Sjölander jump-diffusion model, the Lorentzian *HWHM* is expected to follow [37]:

$$HWHM(Q) = \frac{DQ^2}{1 + DQ^2\tau} \qquad (4)$$

where τ gives the residence time, during which a proton oscillates around an equilibrium position, and D is the jump-diffusion constant, which describes the diffusive motion of a proton from one equilibrium position to another. The jump-diffusion model has been applied before in several studies to describe proteins' internal motions.

The Q-dependence of the elastic incoherent structure factor *EISF* is examined to analyze the geometry of the jump-diffusion process and to calculate the proportion of hydrogen atoms involved. Based on Equation (3), the *EISF* can be calculated as follows:

$$EISF = \frac{A_0(Q)}{A_0(Q) + A_1(Q)} \qquad (5)$$

which is the ratio of purely elastic intensity and the total intensity [39]. The experimentally determined *EISF* has been compared to the theoretical functions for different models. The dependence of the *EISF* on momentum transfer Q can be described by a 4-fold jump-diffusion model, which is a uniaxial rotational jump model between four sites equally spaced on a circle of radius r, according to [35]:

$$EISF = f\frac{1}{4}[1 + 2j_0(Qr\sqrt{2}) + j_0(2Qr)] + (1 - f) \qquad (6)$$

with j_0 being the spherical Bessel function of the zero order, r is the circle's radius, and f is the fraction of mobile H atoms. QENS spectra were fit using the software OriginPro 8 (OriginLab Corp., Northampton, MA, USA) [40].

2.4. Buffer Subtraction

The QENS signal from a protein in solution includes contributions from the protein and from the solvent. This means that buffer subtraction is necessary to obtain an accurate measurement of the protein component. The first step of buffer subtraction is to measure the pure solvent separately. This is typically done by measuring the sample without the protein present. The contribution from the protein can then be isolated by subtracting the contribution from the solvent. Buffer subtraction has been carried out as described in ref. [37]. As shown in Figure 3, each sample spectrum shows a strong correlation peak at a 2θ value of about 100°, which is also clearly visible in the buffer data. This peak can be mainly attributed to D_2O coherent scattering; however, no such intensity is expected in an incoherent scatterer like a protein. We estimated the OCPs' contribution by buffer subtraction with a scaling factor k such that the correlation peak vanishes and the resulting diffractogram becomes flat, like the vanadium standard.

$$I_{Protein} = I_{Sample} - k \times I_{Buffer} \tag{7}$$

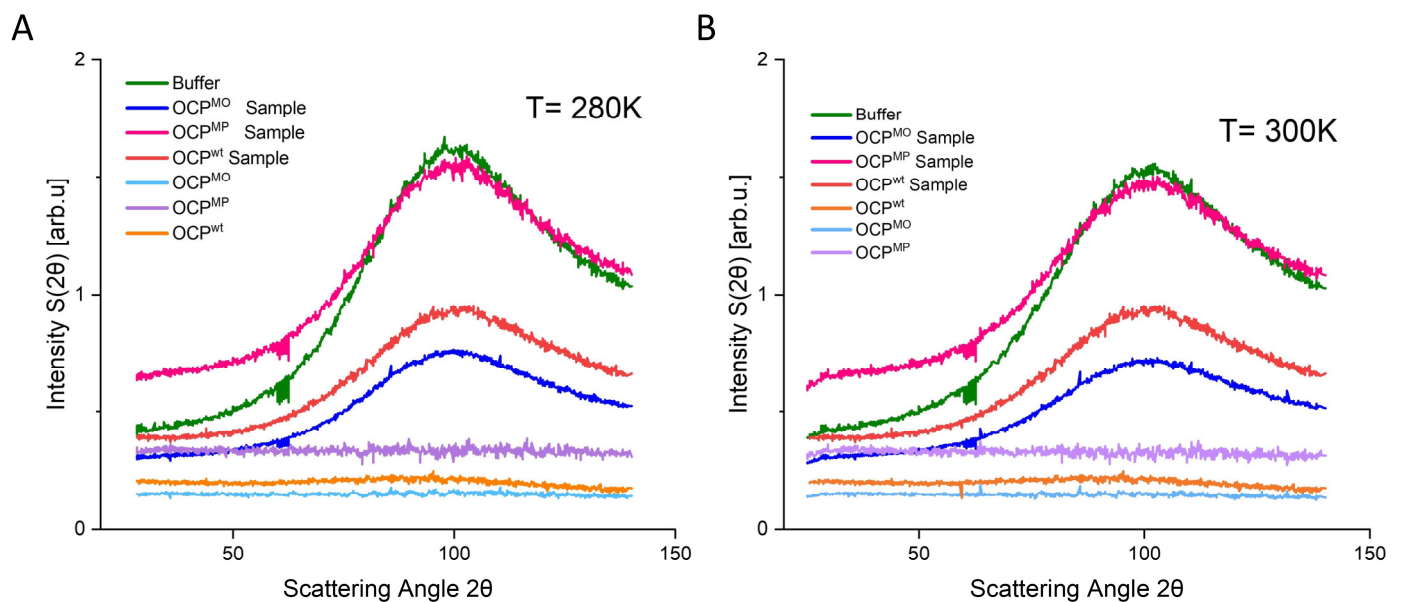**Figure 3.** Buffer subtraction: angle spectra (diffractograms) of OCPs in buffer solution, a separate buffer sample (green line), measured at 280 (**A**) and 300 K (**B**). Each data point is scattering intensity at a specific angle averaged over all neutron energies. The protein contribution is obtained by subtracting the buffer signal from the sample data so that the coherent peak at about 100° vanishes.

In the present case, the scaling factors k for OCP^wt, OCP^MO, and OCP^MP equal 0.8, 0.37, and 0.75, respectively. The resulting QENS spectra are shown in Figure 4.
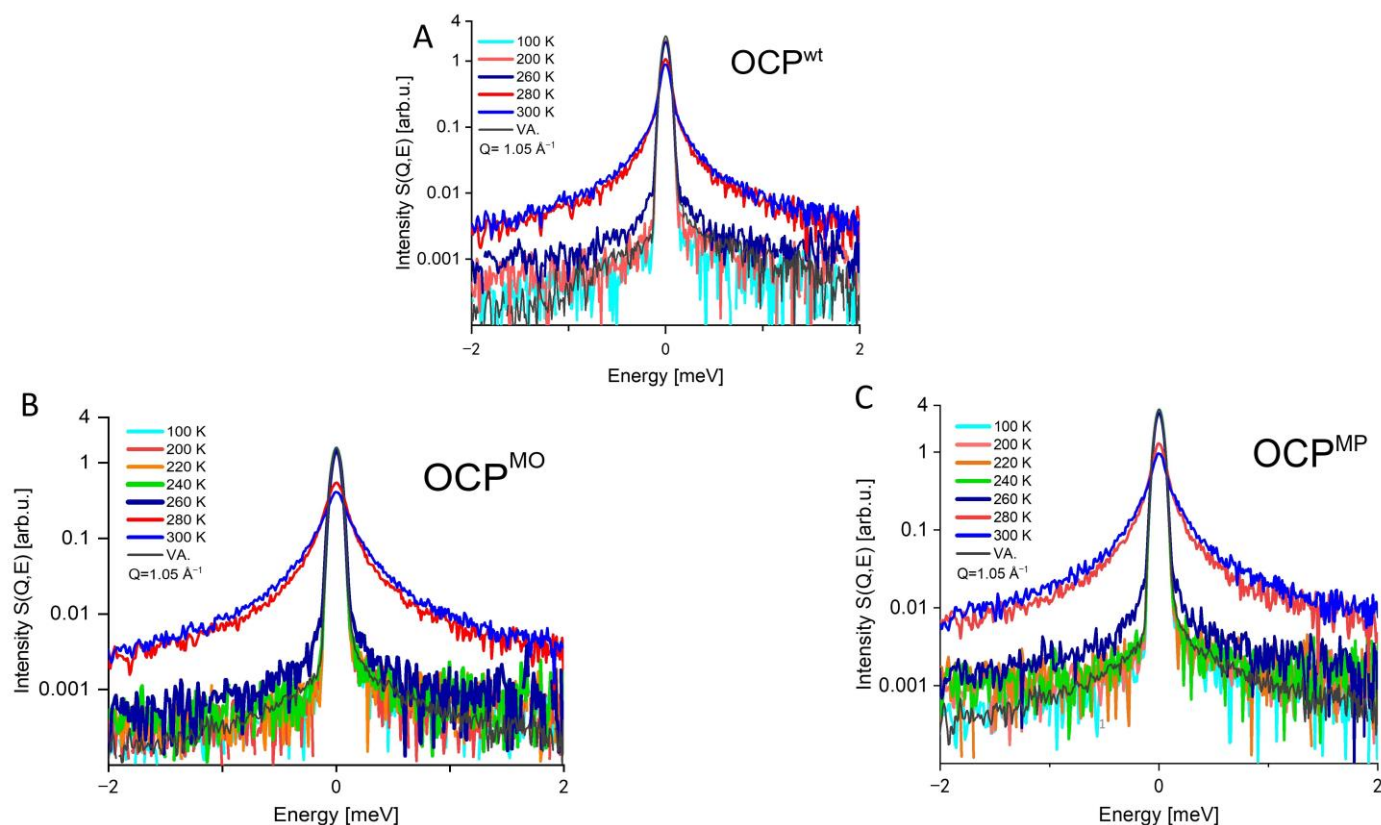
Figure 4. (**A**–**C**) Quasielastic neutron scattering spectra of OCP^{wt} (**A**), OCP^{MO} (**B**), and OCP^{MP} (**C**) were obtained after subtracting the buffer contribution at the different temperatures 100 K, 200 K, 220 K, 240 K, 260 K, 280 K, and 300 K. The instrumental energy resolution determined via vanadium is indicated in A–C (dark brown line). The spectra are summed over all scattering angles, resulting in $Q = 1.05$ Å^{-1}.

3. Results

QENS is a powerful method to directly examine the dynamics of biological samples on the picosecond timescale due to its high sensitivity to incoherent scattering from hydrogen nuclei, which are highly abundant in biological macromolecules [23,27–29]. Figure 4 shows the QENS spectra of three different OCPs (OCP^{wt}, OCP^{MO}, and OCP^{MP}) after normalization by the scaling factor at different temperatures at a selected Q-value of 1.05 Å^{-1}. At low temperatures, the quasielastic contribution is negligible. However, it increases dramatically with rising temperatures. A sizeable quasielastic broadening is already visible at 260 K. All OCPs exhibit a much broader quasielastic contribution at 280 and 300 K above the melting point of D_2O, although OCP^{wt} appears to exhibit a smaller quasielastic contribution than OCP^{MP} and OCP^{MO}. While the elastic signal is caused by static atoms (on the timescale of the QENS experiment), the quasielastic signal is related to diffusing or reorienting atoms.

One elastic Gaussian (gray line) and one Lorentzian (dashed olive line) were sufficient to fit the broadening at temperatures below the melting point of D_2O (see Figure 5A,B). In contrast, the data at higher temperatures (280, 300 K) require a fit by one elastic function (gray line) and two separate Lorentzians (dashed blue and dotted-dashed olive lines; Figure 5C,D). The solid red line in Figure 5 represents the total sum of the Lorentzian functions convoluted with the instrumental resolution [39].
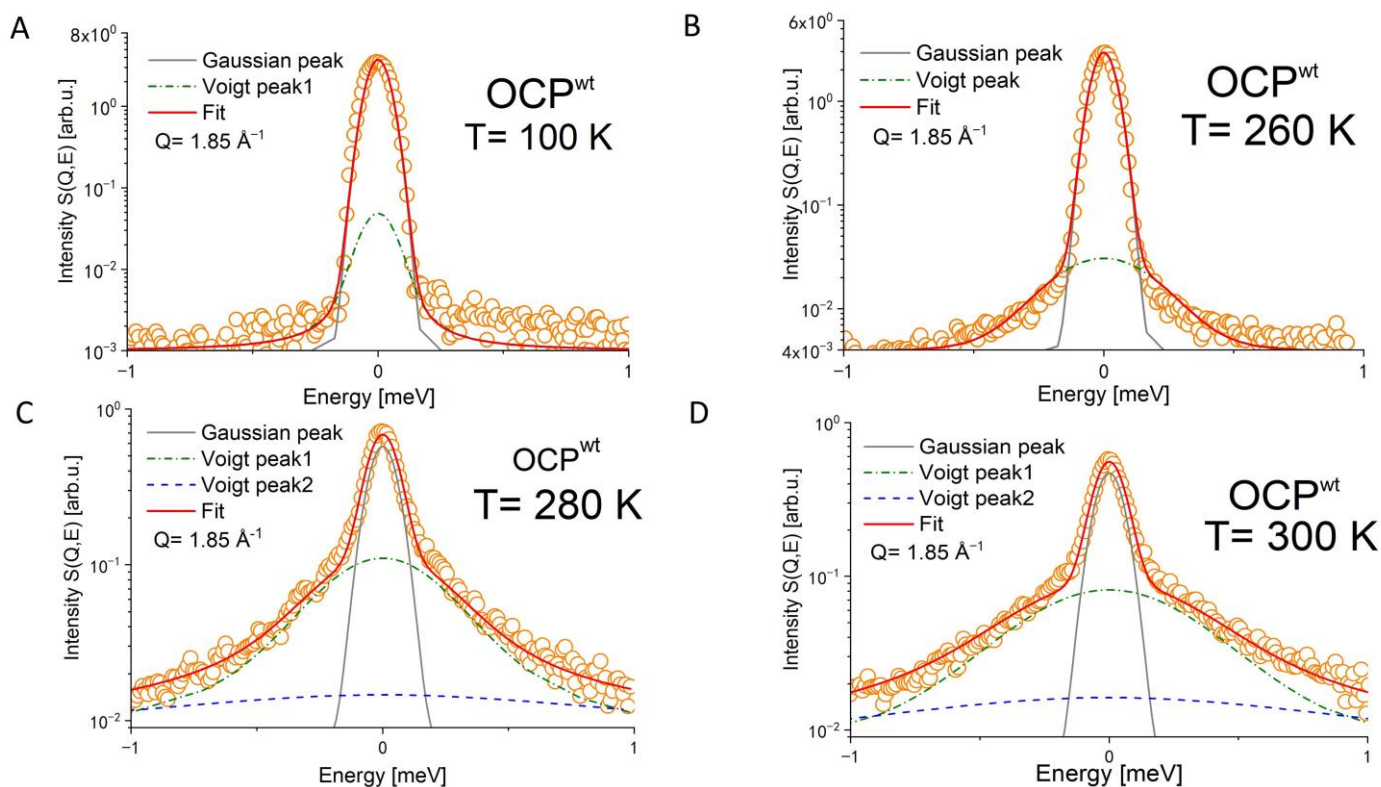
Figure 5. Example of a theoretical fit for the case of the OCP^{wt} QENS spectrum (orange dots) at a representative momentum transfer value Q of 1.85 Å^{-1}, at different temperatures (**A–D**). The elastic contribution is shown as a solid grey line, and the two quasi-elastic (Voigtian) contributions are shown as olive-dotted-dashed and dashed blue lines, respectively. The final fit is shown as a red line. Attempts to decompose the quasi-elastic scattering into two independent Lorentzian components were unsuccessful.

The Lorentzian function, L (ω, Γ), and its half-width at half-maximum (*HWHM*), provide a direct measurement of the timescale of motion, τ. Generally, one can say that faster dynamics are related to wider Lorentzian linewidths, so a broader Lorentzian function typically describes faster atomic motions, while a narrower Lorentzian function describes slower motions [41]. For all low temperatures (100–260 K), the *HWHM* of the single Lorentzian does not exhibit a dependence on Q, so fixed HWHMs were employed in further analysis. The same applies to the broader Lorentzian employed at temperatures of 280 and 300 K (see Table 1 for parameters). This is consistent with localized motions, particularly the rotational or orientational motions of small protein sidechains.

Table 1. Fixed *FWHM* value [meV] for Voigt peak.

Temperature	OCP^{wt} FWHM [meV]	OCP^{MO} FWHM [meV]	OCP^{MP} FWHM [meV]
100 K	0.04	0.10	0.15
200 K	0.04	0.13	0.17
220 K	0.04	0.15	0.22
240 K	0.04	0.18	0.25
260 K	0.09	0.2	0.27

In contrast, the narrower Lorentzian component obtained at 280 and 300 K shows a pronounced Q dependence. Figure 6 presents the dependence of the *HWHM* of the

narrower Lorentzian on the square of the momentum transfer (Q^2) at 280 and 300 K, which is qualitatively consistent with a jump-diffusion model; see below.
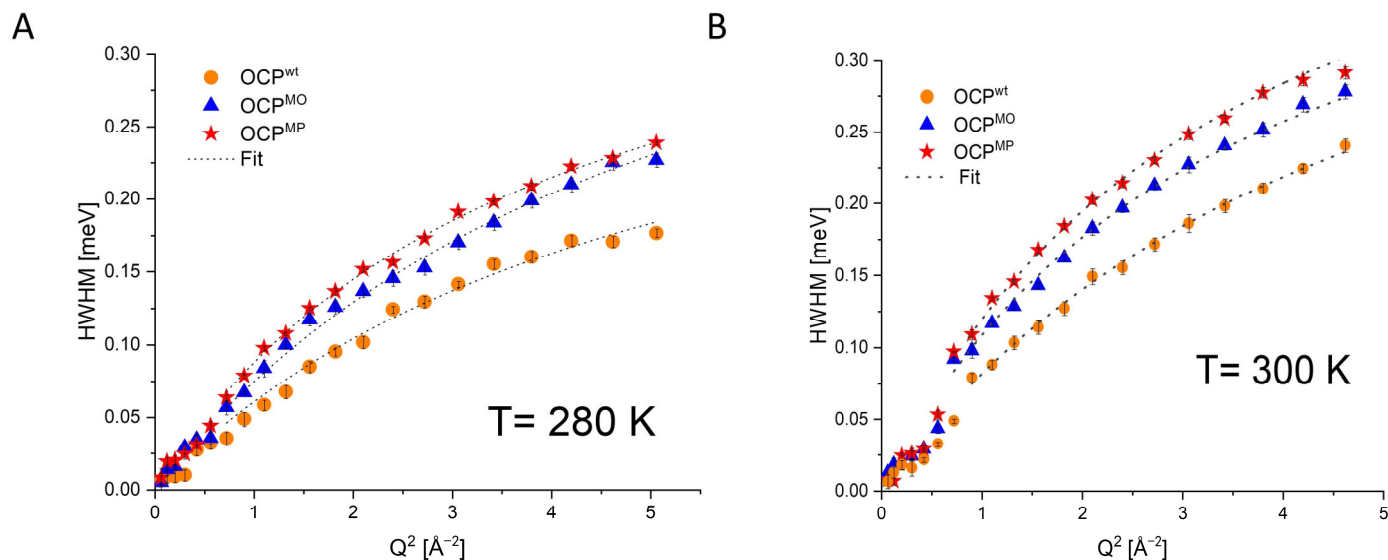

Figure 6. HWHM of the Lorentzian function describes the internal motions as a function of Q^2 of OCP^{wt} (yellow circles), OCP^{MO} (blue triangles), and OCP^{MP} (red stars) at different temperatures, 280 K (**A**) and 300 K (**B**). The parameters of jump-diffusion fits are summarized in Table 1. The fitting has been fixed in Q ranges $1 \leq Q^2\text{Å}^{-2} \geq 5$.

The HWHM Q dependence at 280 and at 300 K can be successfully described using a jump-diffusion model; see Figure 6 and Table 2. Compared with the mutants OCP^{MP} and OCP^{MO} at both 280 and 300 K, the wild-type OCP^{wt} has the lowest HWHM at all Q values. OCP^{wt} also has the smallest jump-diffusion constant (*D*= 1.04 × 10^{-5} and 1.61 × 10^{-5} cm^2/s for 280 and 300 K, respectively). The residence times τ for all three samples at 300 K are generally shorter than those obtained at 280 K. Consistent with the results for D, OCP^{wt} (1.6 and 1.52 ps for 280 and 300 K, respectively) has a higher τ-value than OCP^{MO} (1.55 and 1.43 ps for 280 and 300 K, respectively) and OCP^{MP} (1.46 and 1.38 ps for 280 and 300 K, respectively). This is in line with the generally lower flexibility expected for OCP^{wt} because of its more compact structure than that of the mutant OCP^{MP}. Therefore, especially external protein residues have a lower freedom of motion, and in the case of OCP^{wt} [36,37].

Table 2. Dynamical parameters extracted from the fits of *EISF* and *HWHM* data of the narrow Lorentzian component.

	OCP$^{wt}_{280°}$	OCP$^{MO}_{280°}$	OCP$^{MP}_{280°}$	OCP$^{wt}_{300°}$	OCP$^{MO}_{300°}$	OCP$^{MP}_{300°}$
F	0.547 ± 0.006	0.687 ± 0.015	0.744 ± 0.016	0.633 ± 0.003	0.854 ± 0.007	0.930 ± 0.010
r [Å]	1.274 ± 0.021	1.363 ± 0.039	1.440 ± 0.041	1.501 ± 0.012	1.59 ± 0.016	1.620 ± 0.022
D [meV^2]	0.069 ± 0.004	0.094 ± 0.001	0.105 ± 0.002	0.106 ± 0.001	0.142 ± 0.002	0.167 ± 0.002
Γ [meV^{-1}]	2.437 ± 0.229	2.36 ± 0.094	2.22 ± 0.056	2.316 ± 0.067	2.182 ± 0.023	2.110 ± 0.03
D [10^{-5} cm^2/s]	1.04	1.42	1.59	1.61	2.21	2.25
τ [ps]	1.6	1.55	1.46	1.52	1.43	1.38

It is remarkable, however, that the QENS spectra of OCP^{MP} reveal a larger HWHM than those of OCP^{MO}. In addition, OCP^{MP} is also characterized by a higher diffusion constant *D* (1.59 × 10^{-5} and 2.25 × 10^{-5} cm^2/s for 280 and 300 K, respectively) than OCP^{MO} (1.2 × 10^{-5} cm^2/s and 2.21 × 10^{-5} cm^2/s for 280 and 300 K, respectively). These findings indicate that OCP^{MP} has an even higher flexibility than OCP^{MO}, suggesting that there are structural differences between these two OCP mutants.

The *EISF*, which defines the geometry of a molecular motion, was calculated using Equation (5). In Figure 7, the *Q* dependence of the *EISF* of all three samples is displayed. The *EISF* of all OCPs at lower temperatures (100, 200, 220, 240 K) shows much less variation with *Q* than that observed at higher temperatures (260, 280, and 300 K), suggesting a smaller fraction of mobile hydrogen at low temperatures. The EISFs obtained at 260, 280, and 300 K exhibit a clear *Q* dependence, so a more significant fraction of hydrogen atoms appears to participate in the observed diffusive dynamics [36,37]. Modeling the dependence of *EISF* on Q yields more valuable results regarding the mechanism of the latter dynamics. The dotted black lines also plotted in Figure 7 are the theoretical *EISF* values, calculated using a jump model for four-fold rotational jumps according to Equation (6), which yield the residence time τ of the three OCP forms [42].
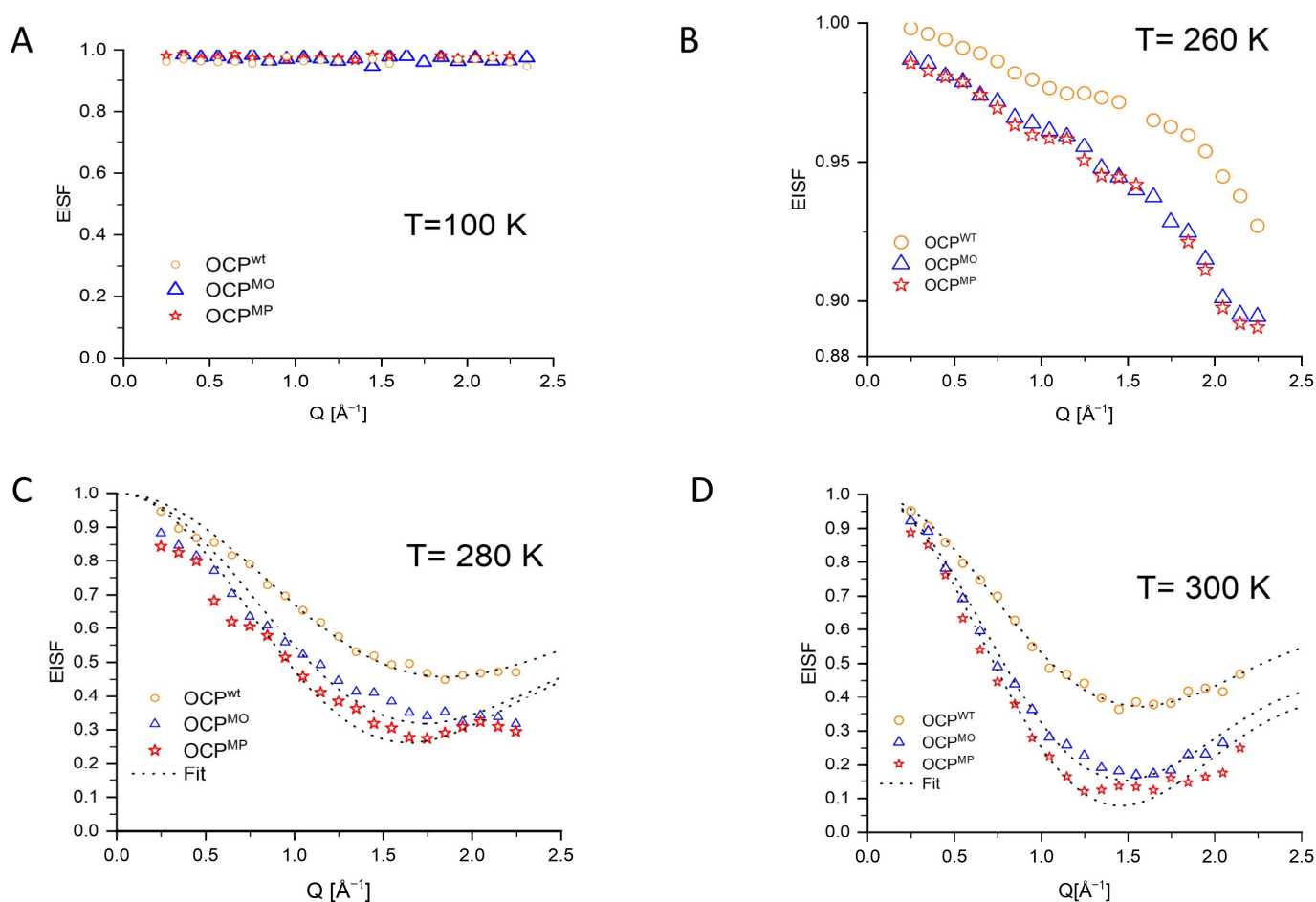

Figure 7. Comparison of elastic incoherent structure factor (*EISF*) from Lorentzian fits of QENS spectra of OCP^{wt} (yellow circles), OCP^{MO} (blue triangles), and OCP^{MP} (red stars) at different temperatures 100 K (**A**), 260 K (**B**), 280 K (**C**), and 300 K (**D**) as a function of momentum transfer Q. The parameters of the fits are summarized in Table 1.

In summary, the *EISF* is generally constant and close to one, see Figure 7A, mainly indicating elastic scattering, possibly due to immobile hydrogen atoms. Changes are noticeable at 260 K, when the EISF starts to show a decay with increasing Q. As discussed above, the latter decay is more pronounced for the two mutant samples, indicating a higher flexibility than observed for the wild type. At higher temperatures, the EISF exhibits a drastic decrease with increasing Q consistent with a much higher flexibility above the melting point of the solvent. Again, the decay of the EISF with increasing Q is more pronounced in the cases of the mutant samples. These conclusions are also supported by the observation of a lower mobile fraction of scatterers of OCP^{wt} (F = 0.55) compared with

OCP^{MO} (0.68) and OCP^{MP} (0.74); see Table 2. In addition, the radii of the jump diffusion are smaller for OCP^{wt} (r = 1.27 Å) than for OCP^{MO} and OCP^{MP} (1.36 and 1.44 Å, respectively).

Figure 8 shows the natural logarithm of the integrated intensity in the OCP^{wt}, OCP^{MO}, and OCP^{MP} elastic peak regions as a function of the square of the momentum transfer Q^2. The data sets exhibit a linear dependence in the lower Q range that can be used to determine the average atomic mean square displacement $<u^2>$ from the slope of a linear fit; see Table 2. The higher slope observed for the mutant samples OCP^{MP} and OCP^{MO} ($<u^2>$ = 0.54 and 0.46, respectively at 280 K) corresponds again to a higher mobility of the mutant OCPs, characterized by a more open structure with separated domains as compared with the more compact wild-type OCP^{wt} ($<u^2>$ = 0.32 at 280 K).
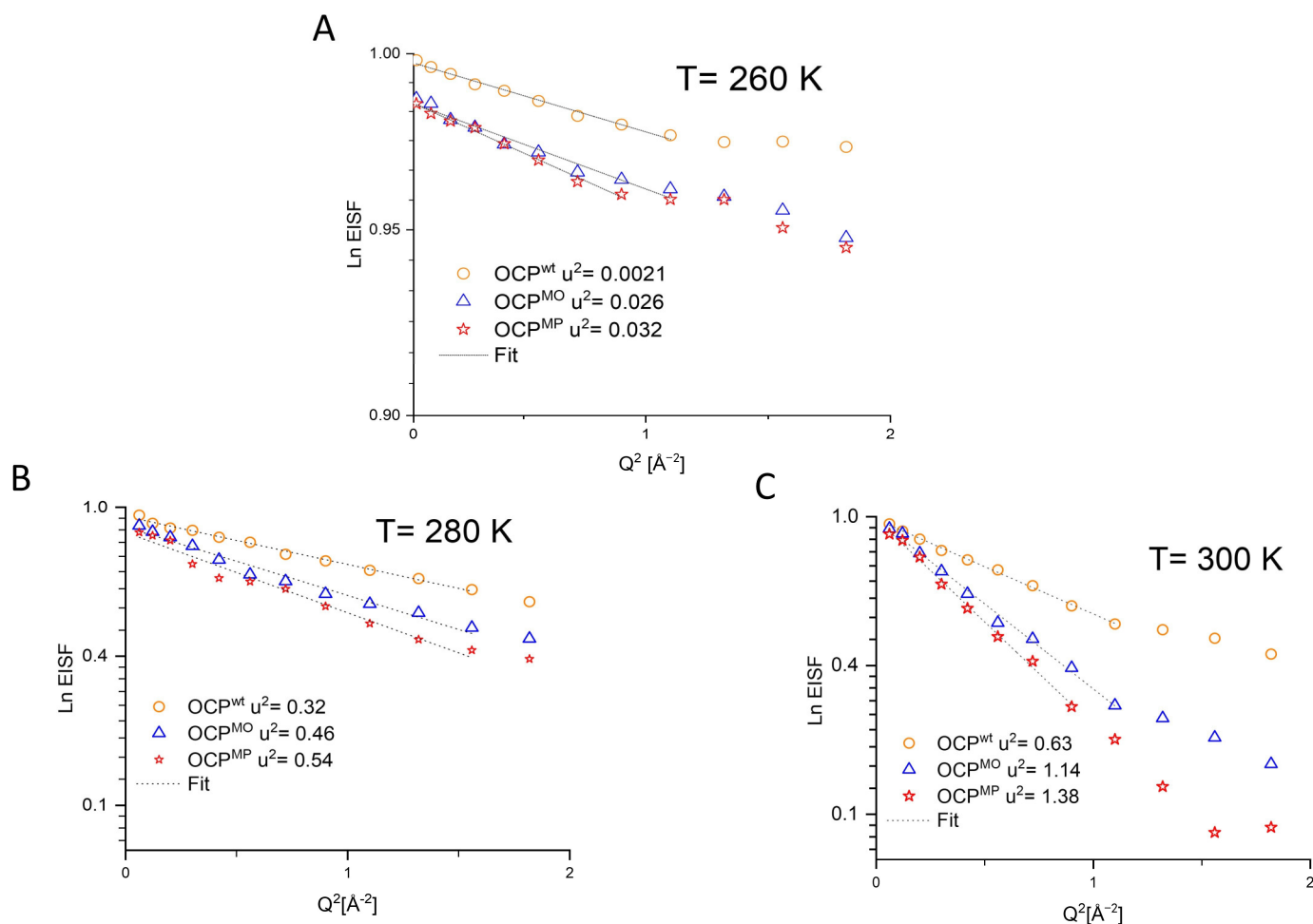

Figure 8. Determination of the average atomic mean square displacements $<u^2>$ of OCP^{wt} (yellow circles), OCP^{MO} (blue triangles), and OCP^{MP} (red stars) at different temperatures 260 K (**A**), 280 K (**B**), and 300 K (**C**): logarithmic plot of the elastic intensities of QENS spectra as a function of momentum transfer Q^2. Linear fits of the data in the low Q-limit are shown as black dots.

4. Discussion

We carried out a thorough investigation of the dynamics of three different forms of OCP over a wide temperature range. Figure 9 shows the temperature dependence of the $<u^2>$-values and QISFs of all three OCP forms obtained. Consistent with our previous studies [36,37], the compact, dark-adapted form OCP^{wt} appears to have a lower flexibility at physiological temperatures (300 K) than the two mutants, especially compared to that with an elongated structure similar to that of the active state. The dynamics of all three OCP forms appear to increase with temperatures above about 200 K (Figure 9C), but do so more drastically above the melting point of the solvent (Figure 9B). Furthermore, there is also a difference in dynamics between the two mutant OCP forms; see below. The latter

observations are fully consistent with the dynamical parameters determined from the model-dependent fits above (see Table 2).
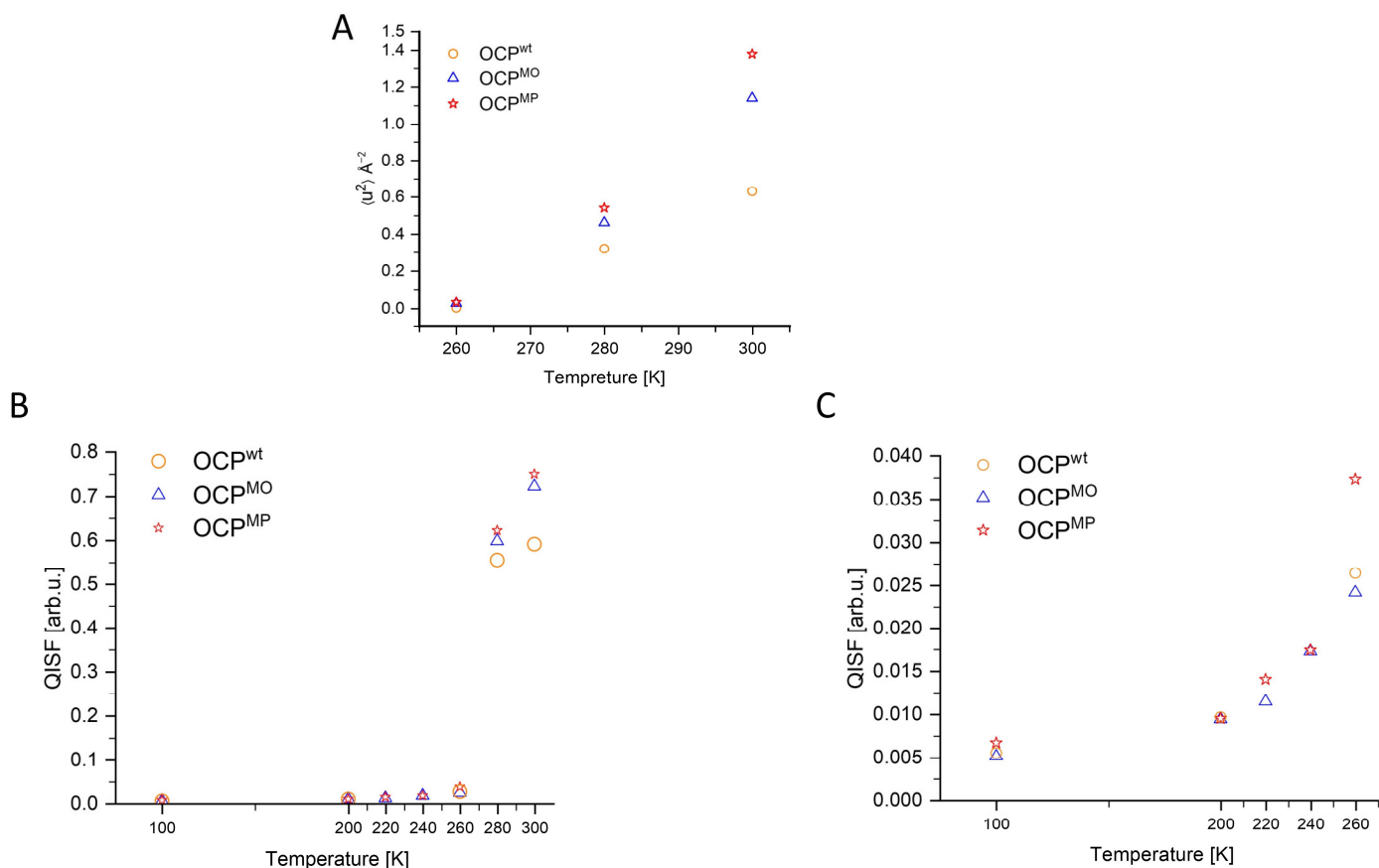

Figure 9. Temperature dependence of the mean square displacement $\langle u^2 \rangle$ (**A**) and QISF (**B**) of OCP^{wt} (yellow circles), OCP^{MO} (blue triangles), and OCP^{MP} (red stars) at different temperatures for QENS data averaged over all scattering angles. Panel (**C**) shows a magnification of the data of Panel (**B**) in the temperature range below the melting point of the solvent.

4.1. Difference between Dynamics of OCP Wild Type and Mutants

The differences in OCP dynamics have to be understood in terms of the structural differences between OCP^{wt} and the mutant form OCP^{MP}, which is expected to possess a structure similar to that of the active state OCP^{R} mainly characterized by a separation of CTD and NTD domains as well as by an unfolding of the NTE (see Figure 1C). These structural changes lead to a larger protein surface and hydration of OCP in general, which can be assumed to permit a higher freedom of motion of the solvent-exposed protein side chains. In addition, the unfolding of the NTE and of the interdomain linkers may be responsible for an increased flexibility of the protein backbone [36,37]. The latter increased protein dynamics may bear significant functional relevance, because a certain flexibility of OCP in the active state may be necessary to adapt the structure of OCP^{R} in solution [14] to that necessary to bind to the PBSs [22].

Furthermore, the QISF and <u^2> data show the thermally activated dynamics of all three OCP forms above 200 K (Figure 9C). This indicates that even below the freezing point of the solvent, the protein residues retain a certain degree of dynamics, suggesting that the hydration layer surrounding the protein is supercooled, thus allowing for interactions between the solvent and the protein residues even in the presence of ice [43]. Nevertheless, the dynamics of all OCP forms appear to be significantly restricted below the freezing point of the solvent at about 276 K. The latter effect can be rationalized by assuming that the formation of ice crystals in the solvent leads to a freeze-concentrated protein or ice-induced crowding similar to aggregation, which can be assumed to restrict protein

dynamics. Therefore, we propose that the low QISF values corresponding to rather rigid OCP in solution at temperatures below ~276 K can be attributed to the restriction of protein dynamics due to ice-induced aggregation [43]. This congestion thus leads to a noticeable reduction in the observed QISF and $<u^2>$ (Figure 9).

4.2. Difference between the Dynamics of OCP Mutants

At higher temperatures of 280 K and 300 K, the QISF of OCP^{MO} appears to be larger than that of OCP^{wt}, but smaller than that of OCP^{MP}. As the temperature increases toward 300 K, there is also a notable increase in the fraction of mobile hydrogens (Figure 7, Table 2). Simultaneously, there is a slight decrease in the correlation time of the jump, indicating a faster dynamics in the case of OCP^{MP}. For instance, the residence time τ decreases from 1.6 ps at 280 K to 1.52 ps at 300 K in the case of OCP^{MP}, which is lower than the respective values for both OCP^{MO} and OCP^{wt}, as compiled in Table 2.

This means that also the mutant OCP^{MO}, which is expected to have a compact structure similar to the dark-adapted state OCP^{O} (see Figure 1B), shows a larger flexibility than OCP^{wt}. This effect can only be rationalized when assuming that the point mutation W288A leading to the absence of one H-bond between protein backbone and pigment affects the stability of the protein in a wider range around the mutation site and, thus, results in a higher flexibility of the whole protein. A similar effect was reported in ref. [36]. The different dynamics of OCP^{MP} and OCP^{MO}, however, are likely to originate from their different structures, although there is no high-resolution structural information available. Illustrative structural models based on SAXS data are shown in Figure 1.

However, OCP^{MP} and OCP^{MO} also differ by the number of carbonyl groups of their carotenoid molecules. Here, CAN, having two carbonyl groups, may form two hydrogen bonds with surrounding water molecules. As a result, OCP^{MP} provides an environment where more hydrogen bonds with highly flexible hydration water can be formed, thereby enhancing the overall dynamics of the protein. In contrast, ECN bound by OCP^{MO} forms rather strong hydrogen bonds with the protein, thus plausibly leading to reduced system dynamics. Hydrogen bonding with hydration water is known to be a pivotal factor influencing the dynamics of proteins. These hydrogen bonds serve as dynamic bridges that connect the protein and its surrounding aqueous environment, influencing the system's overall mobility and stability. Hydrogen bonds form, break, and reform during molecular motions, significantly affecting the ability of the protein to change its structure. Thus, anharmonic and diffusive motions essential for structural relaxation are closely related to the dynamic behavior of hydrogen bonds between the protein and water molecules [44]. In turn, a hydrophobic solute's presence would slow the motion of nearby water molecules by hindering their rotational relaxation without significantly altering the water's structure or hydrogen-bonding strength [45]. Consequently, the hydrogen bonding of CAN with the solvent may contribute to an increase in dynamics in OCP^{MP} besides the structural differences between the mutants.

References

1. Lokstein, H.; Renger, G.; Gotze, J.P. Photosynthetic Light-Harvesting (Antenna) Complexes-Structures and Functions. *Molecules* **2021**, *26*, 3378. [CrossRef] [PubMed]
2. Wilson, A.; Andreeva, E.A.; Nizinski, S.; Talbot, L.; Hartmann, E.; Schlichting, I.; Burdzinski, G.; Sliwa, M.; Kirilovsky, D.; Colletier, J.P. Structure-function-dynamics relationships in the peculiar PCC7805 OCP1: Impact of his-tagging and carotenoid type. *Biochim. Biophys. Acta (BBA)—Bioenerg.* **2022**, *1863*, 148584. [CrossRef] [PubMed]
3. Khorobrykh, S.; Havurinne, V.; Mattila, H.; Tyystjarvi, E. Oxygen and ROS in Photosynthesis. *Plants* **2020**, *9*, 91. [CrossRef]
4. Slonimskiy, Y.B.; Zupnik, A.O.; Varfolomeeva, L.A.; Boyko, K.M.; Maksimov, E.G.; Sluchanko, N.N. A primordial Orange Carotenoid Protein: Structure, photoswitching activity and evolutionary aspects. *Int. J. Biol. Macromol.* **2022**, *222*, 167–180. [CrossRef] [PubMed]
5. Vialet-Chabrand, S.; Matthews, J.S.; Simkin, A.J.; Raines, C.A.; Lawson, T. Importance of Fluctuations in Light on Plant Photosynthetic Acclimation. *Plant Physiol.* **2017**, *173*, 2163–2179. [CrossRef] [PubMed]
6. Kirilovsky, D.; Kerfeld, C.A. The orange carotenoid protein in photoprotection of photosystem II in cyanobacteria. *Biochim. Biophys. Acta* **2012**, *1817*, 158–166. [CrossRef] [PubMed]
7. Adir, N.; Bar-Zvi, S.; Harris, D. The amazing phycobilisome. *Biochim. Biophys. Acta (BBA)—Bioenerg.* **2020**, *1861*, 148047. [CrossRef] [PubMed]
8. Niyogi, K.K.; Truong, T.B. Evolution of flexible non-photochemical quenching mechanisms that regulate light harvesting in oxygenic photosynthesis. *Curr. Opin. Plant Biol.* **2013**, *16*, 307–314. [CrossRef] [PubMed]
9. Leccese, S.; Onfroy, T.; Wilson, A.; Kirilovsky, D.; Casale, S.; Guira, S.; Selmane, M.; Jolivalt, C.; Mezzetti, A. Immobilization of Orange Carotenoid Protein on mesoporous silica SBA-15 for the development of photoactivable nanodevices. *Microporous Mesoporous Mater.* **2022**, *340*, 112007. [CrossRef]
10. Kirilovsky, D.; Kerfeld, C.A. The Orange Carotenoid Protein: A blue-green light photoactive protein. *Photochem. Photobiol. Sci.* **2013**, *12*, 1135–1143. [CrossRef]
11. Wilson, A.; Muzzopappa, F.; Kirilovsky, D. Elucidation of the essential amino acids involved in the binding of the cyanobacterial Orange Carotenoid Protein to the phycobilisome. *Biochim. Biophys. Acta (BBA)—Bioenerg.* **2022**, *1863*, 148504. [CrossRef]
12. Sluchanko, N.N.; Slonimskiy, Y.B.; Moldenhauer, M.; Friedrich, T.; Maksimov, E.G. Deletion of the short N-terminal extension in OCP reveals the main site for FRP binding. *FEBS Lett.* **2017**, *591*, 1667–1676. [CrossRef]
13. Chukhutsina, V.U.; van Thor, J.J. Molecular activation mechanism and structural dynamics of orange carotenoid protein. *Physchem* **2022**, *2*, 235–252. [CrossRef]
14. Golub, M.; Moldenhauer, M.; Schmitt, F.J.; Feoktystov, A.; Mandar, H.; Maksimov, E.; Friedrich, T.; Pieper, J. Solution Structure and Conformational Flexibility in the Active State of the Orange Carotenoid Protein: Part I. Small-Angle Scattering. *J. Phys. Chem. B* **2019**, *123*, 9525–9535. [CrossRef]
15. Yaroshevich, I.A.; Maksimov, E.G.; Sluchanko, N.N.; Zlenko, D.V.; Stepanov, A.V.; Slutskaya, E.A.; Slonimskiy, Y.B.; Botnarevskii, V.S.; Remeeva, A.; Gushchin, I.; et al. Role of hydrogen bond alternation and charge transfer states in photoactivation of the Orange Carotenoid Protein. *Commun. Biol.* **2021**, *4*, 539. [CrossRef]
16. Chukhutsina, V.U.; Baxter, J.M.; Fadini, A.; Morgan, R.M.; Pope, M.A.; Maghlaoui, K.; Orr, C.M.; Wagner, A.; van Thor, J.J. Light activation of Orange Carotenoid Protein reveals bicycle-pedal single-bond isomerization. *Nat. Commun.* **2022**, *13*, 6420. [CrossRef]
17. Liguori, N.; Van Stokkum, I.H.M.; Muzzopappa, F.; Kennis, J.T.M.; Kirilovsky, D.; Croce, R. The molecular origin of the OCP-dependent non-photochemical quenching mechanism in cyanobacteria. *ChemRxiv* **2022**, *1*, 1–26. [CrossRef]
18. Thurotte, A.; Lopez-Igual, R.; Wilson, A.; Comolet, L.; Bourcier de Carbon, C.; Xiao, F.; Kirilovsky, D. Regulation of Orange Carotenoid Protein Activity in Cyanobacterial Photoprotection. *Plant Physiol.* **2015**, *169*, 737–747. [CrossRef]
19. Nizinski, S.; Wilson, A.; Uriarte, L.M.; Ruckebusch, C.; Andreeva, E.A.; Schlichting, I.; Colletier, J.P.; Kirilovsky, D.; Burdzinski, G.; Sliwa, M. Unifying Perspective of the Ultrafast Photodynamics of Orange Carotenoid Proteins from Synechocystis: Peril of High-Power Excitation, Existence of Different S* States, and Influence of Tagging. *JACS Au* **2022**, *2*, 1084–1095. [CrossRef]
20. Gupta, S.; Guttman, M.; Leverenz, R.L.; Zhumadilova, K.; Pawlowski, E.G.; Petzold, C.J.; Lee, K.K.; Ralston, C.Y.; Kerfeld, C.A. Local and global structural drivers for the photoactivation of the orange carotenoid protein. *Proc. Natl. Acad. Sci. USA* **2015**, *112*, E5567–E5574. [CrossRef]
21. Andreeva, E.A.; Nizinski, S.; Wilson, A.; Levantino, M.; De Zitter, E.; Munro, R.; Muzzopappa, F.; Thureau, A.; Zala, N.; Burdzinski, G.; et al. Oligomerization processes limit photoactivation and recovery of the orange carotenoid protein. *Biophys. J.* **2022**, *121*, 2849–2872. [CrossRef]
22. Dominguez-Martin, M.A.; Sauer, P.V.; Kirst, H.; Sutter, M.; Bina, D.; Greber, B.J.; Nogales, E.; Polivka, T.; Kerfeld, C.A. Structures of a phycobilisome in light-harvesting and photoprotected states. *Nature* **2022**, *609*, 835–845. [CrossRef]
23. Gabel, F.; Bicout, D.; Lehnert, U.; Tehei, M.; Weik, M.; Zaccai, G. Protein Dynamics Studied by Neutron Scattering. *Q. Rev. Biophys.* **2002**, *35*, 327–367. [CrossRef]
24. Sacquin-Mora, S.; Sebban, P.; Derrien, V.; Frick, B.; Lavery, R.; Alba-Simionesco, C. Probing the flexibility of the bacterial reaction center: The wild-type protein is more rigid than two site-specific mutants. *Biochemistry* **2007**, *46*, 14960–14968. [CrossRef]
25. Pieper, J.; Trapp, M.; Skomorokhov, A.; Natkaniec, I.; Peters, J.; Renger, G. Temperature-dependent vibrational and conformational dynamics of photosystem II membrane fragments from spinach investigated by elastic and inelastic neutron scattering. *Biochim. Biophys. Acta (BBA)—Bioenerg.* **2012**, *1817*, 1213–1219. [CrossRef]

26. Nalepa, A.; Malferrari, M.; Lubitz, W.; Venturoli, G.; Mobius, K.; Savitsky, A. Local water sensing: Water exchange in bacterial photosynthetic reaction centers embedded in a trehalose glass studied using multiresonance EPR. *Phys. Chem. Chem. Phys.* **2017**, *19*, 28388–28400. [CrossRef]

27. Kneller, G.R. Quasielastic Neutron Scattering and Relaxation Processes in Proteins: Analytical and Simulation-Based Models. *Phys. Chem. Chem. Phys.* **2005**, *7*, 2641–2655. [CrossRef]

28. Haertlein, M.; Moulin, M.; Devos, J.M.; Laux, V.; Dunne, O.; Forsyth, V.T. Biomolecular Deuteration for Neutron Structural Biology and Dynamics. *Methods Enzymol.* **2016**, *566*, 113–157. [CrossRef]

29. Vural, D.; Hu, X.; Lindner, B.; Jain, N.; Miao, Y.; Cheng, X.; Liu, Z.; Hong, L.; Smith, J.C. Quasielastic Neutron Scattering in Biology: Theory and Applications. *Biochim. Biophys. Acta* **2017**, *1861*, 3638–3650. [CrossRef]

30. Lehnert, U.; Reat, V.; Weik, M.; Zaccai, G.; Pfister, C. Thermal motions in bacteriorhodopsin at different hydration levels studied by neutron scattering: Correlation with kinetics and light-induced conformational changes. *Biophys. J.* **1998**, *75*, 1945–1952. [CrossRef]

31. Fitter, J. The Temperature Dependence of Internal Molecular Motions in Hydrated and Dry Alpha-Amylase: The Role of Hydration Water in the Dynamical Transition of Proteins. *Biophys. J.* **1999**, *76*, 1034–1042. [CrossRef]

32. Pieper, J.; Hauss, T.; Buchsteiner, A.; Renger, G. The Effect of Hydration on Protein Flexibility in Photosystem II of Green Plants Studied by Quasielastic Neutron Scattering. *Eur. Biophys. J.* **2008**, *37*, 657–663. [CrossRef]

33. Golub, M.; Rusevich, L.; Irrgang, K.D.; Pieper, J. Rigid versus Flexible Protein Matrix: Light-Harvesting Complex II Exhibits a Temperature-Dependent Phonon Spectral Density. *J. Phys. Chem. B* **2018**, *122*, 7111–7121. [CrossRef]

34. Ptitsyn, O.B. Molten Globule and Protein Folding. *Adv. Protein Chem.* **1995**, *47*, 83–229. [CrossRef]

35. Rodriguez-Velamazan, J.A.; Gonzalez, M.A.; Real, J.A.; Castro, M.; Munoz, M.C.; Gaspar, A.B.; Ohtani, R.; Ohba, M.; Yoneda, K.; Hijikata, Y.; et al. A switchable molecular rotator: Neutron spectroscopy study on a polymeric spin-crossover compound. *J. Am. Chem. Soc.* **2012**, *134*, 5083–5089. [CrossRef]

36. Golub, M.; Moldenhauer, M.; Schmitt, F.J.; Lohstroh, W.; Friedrich, T.; Pieper, J. Light-Induced Conformational Flexibility of the Orange Carotenoid Protein Studied by Quasielastic Neutron Scattering with In Situ Illumination. *J. Phys. Chem. Lett.* **2023**, *14*, 295–301. [CrossRef]

37. Golub, M.; Moldenhauer, M.; Schmitt, F.J.; Lohstroh, W.; Maksimov, E.G.; Friedrich, T.; Pieper, J. Solution Structure and Conformational Flexibility in the Active State of the Orange Carotenoid Protein. Part II: Quasielastic Neutron Scattering. *J. Phys. Chem. B* **2019**, *123*, 9536–9545. [CrossRef]

38. Arnold, O.; Bilheux, J.-C.; Borreguero, J.M.; Buts, A.; Campbell, S.I.; Chapon, L.; Doucet, M.; Draper, N.; Leal, R.F.; Gigg, M.A. Mantid—Data analysis and visualization package for neutron scattering and μ SR experiments. In *Nuclear Instruments and Methods in Physics Research Section A: Accelerators, Spectrometers, Detectors and Associated Equipment*; Elsevier: Amsterdam, The Netherlands, 2014.

39. Rok, M.; Bator, G.; Zarychta, B.; Dziuk, B.; Repec, J.; Medycki, W.; Zamponi, M.; Usevicius, G.; Simenas, M.; Banys, J. Isostructural phase transition, quasielastic neutron scattering and magnetic resonance studies of a bistable dielectric ion-pair crystal $[(CH_3)_2NH_2]_2KCr(CN)_6$. *Dalton Trans.* **2019**, *48*, 4190–4202. [CrossRef]

40. Stevenson, K.J. Review of OriginPro 8.5. *J. Am. Chem. Soc.* **2011**, *133*, 5621. [CrossRef]

41. NaraseGowda, S.; Brown, C.M.; Tyagi, M.; Jenkins, T.; Dobbins, T.A. Quasi-Elastic Neutron Scattering Studies of Hydrogen Dynamics for Nanoconfined NaAlH4. *J. Phys. Chem. C* **2016**, *120*, 14863–14873. [CrossRef]

42. Tripathi, A.K.; Sahasrabudhe, A.; Mitra, S.; Mukhopadhyay, R.; Gupta, N.M.; Kartha, V.B. QENS and FTIR studies on binding states of benzene molecules adsorbed in zeolite HZSM-5 at room temperature. *Phys. Chem. Chem. Phys.* **2001**, *3*, 4449–4455. [CrossRef]

43. Golub, M.; Koppel, M.; Pikma, P.; Frick, B.; Pieper, J. Dynamics–Function Correlation in Photosystem II: Molecular Dynamics in Solution. *Crystals* **2023**, *13*, 1441. [CrossRef]

44. Tarek, M.; Tobias, D. Role of protein-water hydrogen bond dynamics in the protein dynamical transition. *Phys. Rev. Lett.* **2002**, *88*, 138101. [CrossRef] [PubMed]

45. Grdadolnik, J.; Merzel, F.; Avbelj, F. Origin of hydrophobicity and enhanced water hydrogen bond strength near purely hydrophobic solutes. *Proc. Natl. Acad. Sci. USA* **2017**, *114*, 322–327. [CrossRef]